Simulation of nanoparticle coagulation in radio-frequency C_2H_2/Ar microdischarges*

Xiang-Mei Liu(刘相梅)†, Qi-Nan Li(李奇楠), and Rui Li(李瑞)

School of Science, Qiqihar University, Qiqihar 161006, *China*

(Received 11 November 2015; revised manuscript received 14 February 2016; published online 20 April 2016)

The nanoparticle coagulation is investigated by using a couple of fluid models and aerosol dynamics model in argon with a 5% molecular acetylene admixture rf microdischarges, with the total input gas flow rate of 400 sccm. It co-exists with a homogeneous, secondary electron-dominated low temperature γ-mode glow discharges. The heat transfer equation and flow equation for neutral gas are taken into account. We mainly focused on investigations of the nanoparticle properties in atmospheric pressure microdischarges, and discussed the influences of pressure, electrode spacing, and applied voltage on the plasma density and nanoparticle density profiles. The results show that the characteristics of microdischarges are quite different from those of low pressure radio-frequency discharges. First, the nanoparticle density in the bulk plasma in microdischarges is much larger than that of low pressure discharges. Second, the nanoparticle density of 10 nm experiences an exponential increase as soon as the applied voltage increases, especially in the presheath. Finally, as the electrode spacing increases, the nanoparticle density decreased instead of increasing.

Keywords: nanoparticle coagulation, C_2H_2/Ar discharges, microdischarges

PACS: 52.27.Lw, 52.65.–y, 52.80.Pi **DOI:** 10.1088/1674-1056/25/6/065203

1. Introduction

Microdischarges (MDs) have become the subject of considerable research due to their wide range of possible applications in materials treatment and modification, plasma display panels, radiation sources, microsatellite propellers, and in biomedical and environmental applications.[1,2] Among those applications, the microdischarges showed unique properties, such as highly energetic electrons, non-equilibrium, and different discharge structure characteristics. A stable non-equilibrium plasma at length scales ranging from μm to mm is the most remarkable advantage of MDs, where the plasma quenching effects usually exist. In order to overcome plasma quenching effects, MDs rely on high gas pressure ranging from 100 Torr (1 Torr $= 1.33322 \times 10^2$ Pa) to 1 atm (1 atm $= 1.01325 \times 10^5$ Pa), thus the low breakdown or sustained voltages of a few hundred volts is achieved.[3] Due to the various technological implications of MDs, high-pressure small-scale plasmas become increasingly important. To this effect, a fundamental understanding of the characteristics of atmospheric pressure plasmas and microplasmas is obviously crucial. By experimental measurements and computer simulations,[4–8] several attempts have been made to describe the microplasmas in atmospheric capacitively rf discharges. Babayan *et al.*[4–6] investigated the atmospheric pressure helium rf microdischarges, which are operated at gas temperatures below 100 °C. The results showed that a high density of reactive species is generated and a stable capacitive discharge is produced, which are suitable for the downstream processing of substrates. Iza *et al.*[7,8] demonstrated non-equilibrium characteristics and the highly energetic electrons effects in rf microdischarges. By using DC discharge model, Economou and Radjenovic *et al.*[9,10] investigated the breakdown voltage versus pd scaling, and observed that the cathode layer (sheath) classical scaling law does not apply. Lee *et al.*[11,12] presented two operating modes, α and γ, in atmospheric pressure capacitive discharges, which depends on the dominant ionization process. In γ discharge, the plasma is sustained by secondary electron emission, while in the α discharge, it is sustained by bulk ionization. They showed that the changes of input power and ultra-high frequency are the major causes for the α–γ mode transition.

The behaviors of inert gases, such as Ar and He, are relatively well understood in MDs, but the reactive gases discharge characteristics, such as the C_2H_2/Ar, SiH_4/Ar, and C_2H_2/Ar/H_2 discharge properties are still elusive so far. First, reactive gases discharges can yield highly polymerized ions, and these hydrocarbon–gas mixtures tend to produce dust particles, which will cause structural voids, dislocations, and film delamination which ultimately lead to mal-

*Project supported by the Natural Science Foundation of Heilongjiang Province, China (Grant Nos. A2015011 and A2015010), the Postdoctoral Scientific Research Development Fund of Heilongjiang Province, China (Grant No. LBH-Q14159), the Program for Young Teachers Scientific Research in Qiqihar University (Grant No. 2014k-Z11), the National Natural Science Foundation of China (Grant No. 11404180), and the University Nursing Program for Yong Scholars with Creative Talents in Heilongjiang Province, China (Grant No. UNPYSCT-2015095).

†Corresponding author. E-mail: lxmjsc98@163.com

© 2016 Chinese Physical Society and IOP Publishing Ltd

functioning devices.[13,14] Second, reactive gases discharges are widely used in microelectronics manufacturing and photovoltaic cells.[15,16] Therefore, a detailed investigation of the microplasma species densities, such as electrons, ions, molecules, radicals as well as nanoparticles, together with a comprehensive understanding of their behavior in reactive gases discharge are very necessary. In MDs, with micrometer and submillimeter gaps, the gas pressure is usually very high, thus the secondary electron plays an important role in sustaining the discharge, which is quite different from the low-pressure discharge. Furthermore, the simple parallel-plate configuration instead of the special microhollow electrodes or pin electrodes configurations is found to be sufficient to produce plasma.[17] In this study, we focus our interest on the influence of pressure, power, and gas flow on the nanoparticle formation and growth mechanisms in a C_2H_2/Ar microplasma, where Ar accounts for the vast majority to generate a stable non-equilibrium plasma. In capacitively coupled MDs, the plasma density can be very high and the large-aperture uniform plasma can be obtained, which can be useful in processing.

The structure of this article is as follows. A description of the fluid model and the aerosol physics model are briefly surveyed in Section 2, and the formation, transport, and growth mechanism for nanoparticles are also elaborated. In Section 3, the MDs parameters effects on the plasma and nanoparticles characteristics are carefully discussed. Finally, a short conclusion is described in Section 4.

2. Theoretical model

2.1. Plasma kinetics

In the discharge we considered here, 57 different species and hundreds of chemical reactions must be introduced. Moreover, the nanoparticles are formed by coagulation, thus the particles are relatively small in comparison with the particles formation by other means, for example by introducing externally. Therefore, the fluid model is used to describe the particle formation and growth by nucleation to further growth by agglomeration via a coupling to the aerosol dynamics model.[18,19] In this one-dimensional (1D) fluid model, the continuity balances equations are taken into account to describe the electrons, ions, radicals, and molecules mass density, the momentum equations for electrons, ions, and radicals can be estimated by the drift-diffusion approximation. However, ions' masses are much larger than the electrons', hence the effective electric field is introduced to follow the inertia effects. For neutral gases, the momentum balance equation for axial mass-averaged velocity is introduced to describe the neutral reacting flow. The electrons and neutral gases energy balance equations are introduced to solve the electron temperature and neutral gas temperature. No energy balance equation is included for ions, since the ion pressure plays only a minor role in the momentum equation, the ion temperature is assumed to be a constant. Finally, the Poisson equation is coupled to the particle's balance equations, making the model fully self-consistent.

For every electron-neutral collision the electron mobility and diffusion coefficients, as well as the reaction rate coefficients as a function of the average electron energy, are obtained from the electron energy distribution function (EEDF). However, the EEDF is computed from the Boltzmann equation in a two-term approximation. Table 1 gives the electron impact collisions reactions.

Table 1. Electron impact collisions reactions and the corresponding threshold energies.

Reaction	Threshold energy/eV	Reaction type	Ref.
$e + C_2H_2 \rightarrow C_2H_2^+ + 2e$	11.4	Ionization	[14]
$e + C_2H_2 \rightarrow C_2H^+ + H + 2e$	16.5	dissociative ionization	[14]
$e + C_2H_2 \rightarrow C_2^+ + H_2 + 2e$	17.5	dissociative ionization	[14]
$e + C_2H_2 \rightarrow CH^+ + CH + 2e$	20.6	dissociative ionization	[14]
$e + C_2H_2 \rightarrow C^+ + CH_2 + 2e$	20.3	dissociative ionization	[14]
$e + C_2H_2 \rightarrow H^+ + C_2H + 2e$	18.4	dissociative ionization	[14]
$e + C_2H_2 \rightarrow C_2H + H + e$	7.5	dissociative	[14]
$e + C_2H_2 \rightarrow C_2H^- + H$	2.74	dissociative	[14]
$e + C_4H_2 \rightarrow C_4H + H + e$	7.5	dissociative	[14]
$e + C_6H_2 \rightarrow C_6H + H + e$	7.5	dissociative	[14]
$e + C_8H_2 \rightarrow C_8H + H + e$	7.5	dissociative	[14]
$e + C_{10}H_2 \rightarrow C_{10}H + H + e$	7.5	dissociative	[14]
$e + C_{12}H_2 \rightarrow C_{12}H + H + e$	7.5	dissociative	[14]
$e + C_4H_2 \rightarrow C_4H_2^+ + 2e$	10.19	ionization	[14]
$e + C_6H_2 \rightarrow C_6H_2^+ + 2e$	9.55	ionization	[14]
$e + C_2H_2 \rightarrow H_2CC^-$	2.74	attachment	[14]
$e + C_4H_2 \rightarrow C_4H^- + H$	1.94	dissociative attachment	[14]
$e + C_6H_2 \rightarrow C_6H^- + H$	2.74	dissociative attachment	[14]
$e + C_8H_2 \rightarrow C_8H^- + H$	2.74	dissociative attachment	[14]
$e + C_{10}H_2 \rightarrow C_{10}H^- + H$	2.74	dissociative attachment	[14]
$e + H_2 \rightarrow H_2^+ + 2e$	15.4	ionization	[14]
$e + H_2 \rightarrow H + H + e$	8.9	dissociative	[14]

2.2. Nanoparticle formation

The growth of small gas molecule species to larger molecules which consist of hundreds of atoms are mainly dealt with by the nucleation module.[14] The starting point of nanometer-sized dust grains' formation in acetylene-based plasmas appears to be $C_{12}H^-$ and $C_{12}H_2^-$, which proceed through a series of chemical reactions between anions and acetylene molecules.

$$\begin{aligned} C_2H^- + C_2H_2 &\rightarrow C_4H^- + H_2, \\ C_{10}H^- + C_2H_2 &\rightarrow C_{12}H^- + H_2, \end{aligned} \quad (1)$$

$$\begin{aligned} &H_2CC^- + C_2H2 \rightarrow C_4H_2^- + H_2, \\ &C_{10}H_2^- + C_2H_2 \rightarrow C_{12}H_2^- + H_2, \end{aligned} \quad (2)$$

where H_2CC^- and C_2H^- are taken as the primary anions in our model, which formed from the dissociative electron attachment (DEA) of acetylene

$$e + C_2H_2 \rightarrow C_2H^- + H, e + C_2H_2 \rightarrow H_2CC^-. \quad (3)$$

It has shown that 95% of the production from DEA on C_2H_2 is H_2CC^-, and 5% is C_2H^-.

The larger anions $C_{12}H^-$ and $C_{12}H_2^-$ are used as a source term to form the second stage of particle formation, i.e., coagulation. Thus, the nanoparticle mass density is described by

$$\frac{dn_d}{dt} + \frac{d\Gamma_d}{dx} = J_{nuc} + G_{coag} + G_{sg} + R_{charge}, \quad (4)$$

where the nucleation rate J_{nuc} is the source term to the smallest particle size section, and will disappear in the population balance for any other section. The coagulation coefficient G_{coag} is determined through an integration over the interacting sections and the growth coefficient for coagulation G_{sg} calculated from two smaller sections to a larger section. R_{charge} expresses a charge fluctuations term, which can occur by processes such as secondary electron emission, electron and ion attachment, electron detachment due to collisions with excited atoms or molecules, and UV photodetachment.

2.3. Nanoparticle transport

Nanoparticles immersed in a plasma affected by five different forces, including neutral drag force

$$F_n = -\frac{4}{3}\pi r_d^2 n_n m_n \upsilon_{th} \upsilon_d,$$

electrostatic force $F_E = Q_d E$, gravity

$$F_g = \frac{4}{3}\pi r_d^3 \rho_d g,$$

ion drag

$$F_i = n_i \upsilon_s m_i \upsilon_i \pi b_c^2 + n_i \upsilon_s m_i \upsilon_i 4\pi b_{\pi/2}^2 \Gamma,$$

and the thermophoresis

$$F_{th} = -\frac{32}{15}\frac{r_d^2}{\upsilon_{th}} k_T \nabla T_{gas}.$$

The thermophoresis force is especially important when the neutral gas heat transfer equation is taken into account. The nanoparticles flux Γ_d is obtained by assuming the neutral drag force balances with all the other forces, thus Γ_d can be calculated from Ref. [7]

$$\begin{aligned} \Gamma_d = &-\mu_d n_d E_{eff} - D_d \frac{dn_d}{dx} - \frac{n_d}{\nu_{md}} g \\ &+ \sum \frac{n_d m_i \upsilon_s}{m_d \nu_{md}} \left(4\pi b_{\pi/2}^2 \Gamma + \pi b_c^2\right) \Gamma_i \\ &- \frac{32}{15}\frac{n_d r_d^2}{m_d \nu_{md} \upsilon_{th}} k_T \frac{dT_{gas}}{dx}, \end{aligned} \quad (5)$$

where n_d, r_d, m_d, and ν_{md} are the nanoparticles' density, radius, mass, and momentum loss frequency, μ_d and D_d are mobility and diffusion coefficient for nanoparticles. g is the gravitational acceleration and k_T the thermal conductivity. b_c is the collection impact parameter, and $b_{\pi/2}$ is the impact parameter that corresponds to the deflection angle $\pi/2$. υ_s, υ_{th} are the ion mean speed and average thermal velocity, respectively. m_i is the ion mass and Γ_i is ion flux. Γ is the Coulomb logarithm.

2.4. Nanoparticle coagulation

In the coagulation phase, the particles' size generally increases in time from several nanometers to tens of nanometers, and the particles' density sharply decreased.[7] To this effect, aerosol physics is considered as a good technique for the investigation of coagulation and an excellent assumption for the conditions of interest is used. In this model, the nanoparticle density $n(v)$ in a volume range $(v, v + dv)$ is investigated by the general dynamic equation

$$\begin{aligned} \frac{\partial n(v)}{\partial t} = &\frac{1}{2}\int_0^v \beta(u, v-u) n(v-u) n(u)\, du \\ &- \int_0^\infty \beta(u, v) n(v) n(u)\, du + J_0(v)\delta(v - v_0), \end{aligned} \quad (6)$$

where the particles' formation between two smaller particles in the volume range $(v, v + dv)$ is presented in the first term on the right hand side, while the loss of particles due to coagulation with the other particles is described in the second term on the right hand side. $J_0(v)\delta(v - v_0)$ expresses the new particles formation rate with volume v_0 by nucleation. The coagulation frequency $\beta(u, v)$ between two interacting particles is described in Ref. [7]. Equation (6) is adopted to describe the size distribution evolution of the nanoparticle. In this sectional model, the particle domain is divided logarithmically in some volume sections with their own average charge, mass and radius.

3. Results and discussion

In this article, to investigate the behaviors of a nanoparticle in MDs, a 13.56-MHz radio-frequency source with the peak voltage of 100 V is applied to the upper showerhead electrode, and the lower electrode is grounded. In this rf MDs, the plasma is sustained by the secondary electron emission (SEE), where the secondary electron emission coefficient depends on the state of the electrode surface, the kind of particle, the particle energy which impacts on the electrode, and the electrode material. We investigated the effects of different secondary

electron emission coefficients on the plasma parameters, and observed that SEE coefficients almost have no special effects on the absolute values of the results. Thus, the SEE coefficient is assumed to be $\gamma_{se} = 0.1$. We set the total input flow rate at $F_{tot} = 400$ sccm, with 5% mole fraction of acetylene at 20 sccm. The gas pressure ratio of Ar: C_2H_2=19:1. The ion temperature $T_{ion} = 400$ K and the initial electron temperature $T_e = 3$ eV. The gas distance between two parallel plate electrodes varies from 100 μm to 1000 μm. The gas pressure is in the range of 100 Torr–760 Torr, while the voltage varies from 100 V to 300 V. In this model, the time-step of an RF (13.56 MHz) cycle is set to be 7.4×10^{-13}, and the space-step is 5×10^{-6} m. To speed up the calculation, the time-step for describing the neutral–neutral chemistry is 100 times larger than the RF cycle, while the dust particles' time-step is equal to 7.4×10^{-9}.

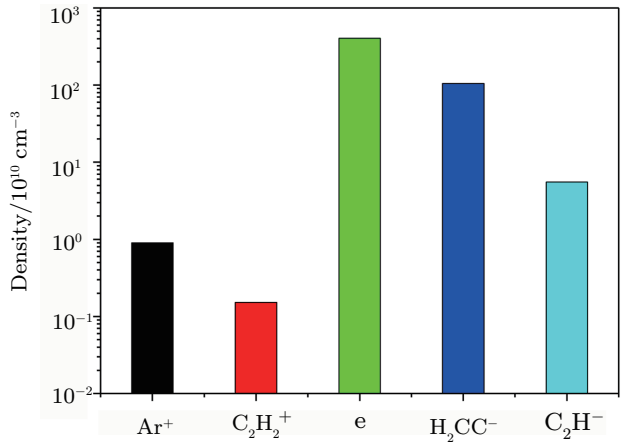


Fig. 1. (color online) The positive ions, negative ions and electron density obtained from our simulation, with $V = 100$ V, $P = 600$ Torr, $L = 1000$ μm.

Figure 1 shows the calculated density of positive ions, electron and negative ions at the centre of the plasma, with the electrode spacing $L = 1000$ μm. It should be noted that the maximum of electron density is about 4×10^{12} cm^{-3}. Opposed to electron density, Ar^+ takes a value of about 1×10^{10} cm^{-3}, meaning that the electron density is around two orders of magnitude larger than the Ar^+ density. This may result from the following two reasons:

(i) Based on Moravej,[20] the ionization coefficient for argon is $4 \times 10^{-12} T_e^{0.5} e^{-15.8/T_e}$ cm^3/s, meaning that Ar^+ is only produced by electron impact collisions on Ar above 15.8 eV, while $C_2H_2^+$ is produced by electron impact collisions on C_2H_2 above 11.4 eV from Ref. [14]. Thus, the ionization coefficient of argon is much smaller than the ionization coefficients of acetylene;

(ii) Acetylene is reactive gas, which will generate a great number of positive ions, around 17 positive ions are taken into account in this paper.

In acetylene discharges, $C_4H_2^+$ is presented as an important positive ion, which reaches a concentration of about 2×10^{11} cm^{-3} in the plasma bulk, approximately 20 times larger than the density of Ar^+. Negative ions H_2CC^- and C_2H^- are the main precursors for the particle formation, since they can be confined in the discharge region on the concerted action of the electrostatic force, the corresponding peaks are 1×10^{12} and 5×10^{10}.

The spatial profiles of the electron temperature (T_e), the ionization coefficient (k_r) for Ar, and the dissociative ionization coefficient (k_{di}) for C_2H_2 are displayed in Fig. 2. As we can see, the electron temperature presents two peaks near the presheath for the electric field effect, but much lower in the plasma bulk around 1.2 eV. In fact, to obtain a stable discharge in microplasmas, a large number of inert gases, such as argon and helium, are required. Thus, the gas pressure ratio of Ar and C_2H_2 is set to 19 in this paper. Since Ar^+ density is much lower than the $C_4H_2^+$ density, which has been described in Fig. 2, some comparison between k_r and k_{di} is made in Fig. 3. We can clearly see that the peak of k_{di} is five orders of magnitude larger than the maximum value of k_r, which finally leads to $C_4H_2^+$ density is a factor of 20 higher than Ar^+ density under the condition of Ar : C_2H_2=19:1. It is worth noticing that the ionization coefficients k_{di} and k_r keep stable values in the plasma region but increase rapidly in the sheath region for the acceleration of the electric field.

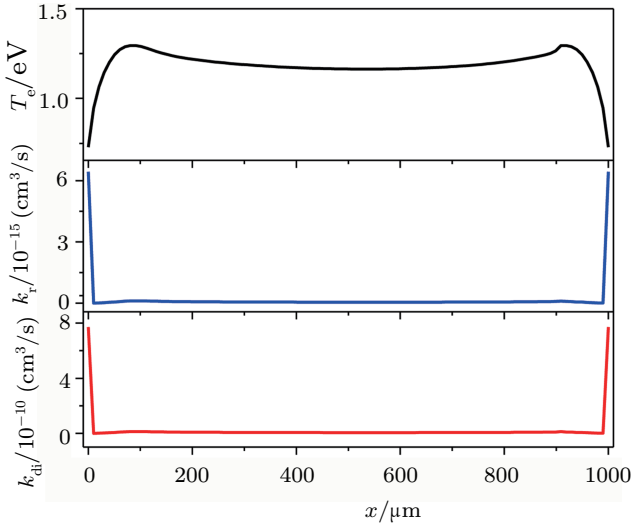


Fig. 2. (color online) The spatial variation profiles of the electron temperature (T_e) and the ionization coefficient (k_r) for Ar, as well as the dissociative ionization coefficient (k_{di}) for C_2H_2, with the settings the same as those in Fig. 1.

Figure 3 shows the spatial profiles of the H_2CC^- density generated through the electron impact attachment on C_2H_2 and the corresponding attachment coefficient k_{da}, effects from different gas pressure, which has been set at 400, 600, and 760 Torr. As we can see, the k_{da} shows little decrease to the gas

pressure while the H_2CC^- density increases sharply with the increasing of gas pressure, indicating that the rising amplitude of the background gas density is much larger than the decrease amplitude of the attachment coefficient. With increasing the pressure, the collisions between background gas (C_2H_2) and electrons become more frequent, and more ions are produced. However, more collision frequency existence will finally lead to the decrease in the electron energy and electron temperature, thus the attachment coefficient k_{da} decreases with the increasing of gas pressure. Moreover, the attachment coefficient exhibits two peaks in the presheaths, but much lower in the bulk plasma; similar distribution has also been observed in the electron temperature. However, the anion H_2CC^- mainly locates in the plasma region under the high-voltage electrostatic field.

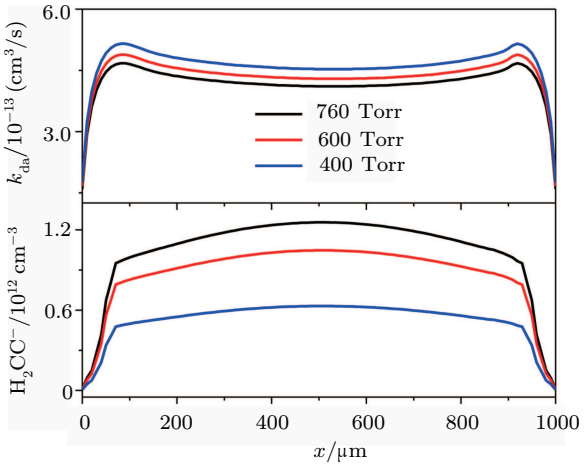


Fig. 3. (color online) The spatial variation profiles of the negative ion (H_2CC^-) and the corresponding attachment coefficient k_{da} at different gas pressure, with $P = 400$, 600, and 760 Torr.

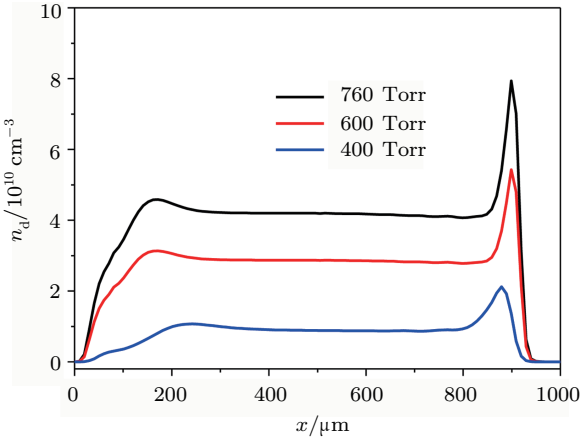


Fig. 4. (color online) The spatial variation profiles of the nanoparticle number density n_d at different gas pressure, with the settings the same as those in Fig. 3.

The effect of gas pressure on the nanoparticles' density n_d is plotted in Fig. 4, with the particle size of 10 nm. It can be clearly seen in Fig. 4 that a local maximum is presented in front of the showerhead electrode, which is due to the fact that the thermophoretic force moves the nanoparticles away from the showerhead electrode to the presheath region where the gradient of the neutral gas temperature is maximum. Compared with our previous studies,[19] the nanoparticle density in the bulk plasma for MDs is much higher, suggesting that more collisions between background gas and electrons occur due to higher gas pressure, and this leads to the increase of nanoparticles and the shrinking in the sheaths. Therefore, the nanoparticles' profile has a great difference between atmospheric pressure microdischarges and low pressure radio-frequency discharges. We can also notice from Fig. 4 that the nanoparticle density increases definitely with the increasing of gas pressure, especially in the presheath region. This is responsible for increases in the collision frequency and plasma density, as well as the neutral gas temperature gradient.

Figure 5 shows the spatial profiles of the negative ion density (H_2CC^-) and the attachment coefficient k_{da} effects from different electrode spacing, with the gas pressure of 600 Torr. We can see from Fig. 5 that H_2CC^- increases with the decreasing of electrode spacing. As is well known, decreasing the electrode spacing tends to expand the sheath to the bulk plasma, and then more secondary electrons can be emitted from the upper and lower electrodes, which leads to the higher plasma density. This result indicates that the electrode spacing has a great effect on the plasma parameters. Evident influences of the electrode spacing on the electron impact collisions can also be seen in Fig. 5. As we can see, the two peaks of k_{da} appear in the presheath region instead of just increasing with the decreasing of electrode spacing, showing that the electrode spacing can not only change the plasma parameters, but also their distribution.

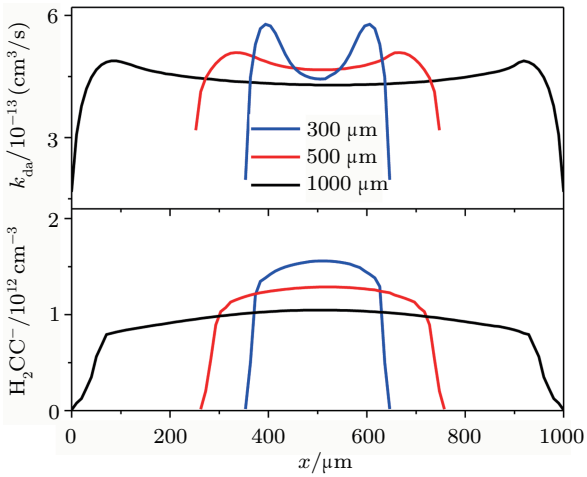


Fig. 5. (color online) The spatial variation profiles of the negative ion (H_2CC^-) and the corresponding attachment coefficient k_{da} at different electrode spacing, with $L = 300$, 500, and 1000 μm.

Figure 6 illustrates the spatial profiles of nanoparticles' density n_d dependent on the electrode spacing, in which the electrode spacing has been set at 300, 500, and 1000 μm. The nanoparticles' size is set at $D_d = 10$ nm, where the nanoparticles can display the coagulation properties. As we can see,

a dominant peak of the nanoparticle density is presented near the upper electrode but much lower concentration in the bulk plasma, showing evidently the neutral gas flow effect. Moreover, similar to Fig. 5, the nanoparticle density in this article greatly depends on the electrode spacing. As the electrode spacing decreases from 1000 μm to 300 μm, the particle density increases by nearly two times. This is due to the fact that the important precursor density (H_2CC^-) of the dust formation increases with the decreasing of electrode spacing, which drives the nanoparticle density increases. These results are quite different from the low pressure rf discharge, since the gas ionization is dominated by the secondary electron emission in the MDs, while the low pressure rf discharge is mainly sustained by the bulk plasma electrons collisions.

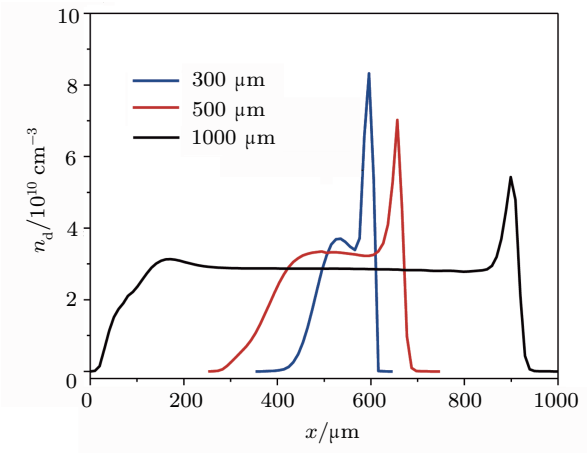


Fig. 6. (color online) The spatial variation profiles of the nanoparticle number density n_d at different electrode spacing, with the settings the same as those in Fig. 5.

Figure 7 presents the spatial profiles of the negative ion density (H_2CC^-) and the attachment coefficient k_{da}, depending on the applied voltage, with the voltage set at 100, 200, and 300 V. It can be seen that, the attachment coefficient k_{da} and the density of H_2CC^- dramatically increases with the increasing of the applied voltage, especially the H_2CC^- density increases exponentially. In this article, secondary electron emission is responsible for the electron heating, thus the input voltage and power are mainly dissipated by the secondary electrons. In other words, as the voltage increases, more secondary electrons can be emitted from the electrodes, resulting in an increase in the attachment efficiency and plasma density. Thus, H_2CC^- density in the bulk plasma increases deeply with the applied voltage, whereas the attachment coefficient increases slightly. The voltage effect on the nanoparticle density n_d is also investigated, which has been plotted in Fig. 8. Similar to the results of H_2CC^- density, the nanoparticle density at the size of 10 nm increases greatly with the increasing of the applied voltage, especially at the peak region, suggesting high gas temperature gradient effect. We can conclude that the applied voltage has a great impact on the plasma density and even the nanoparticles' formation and growth.

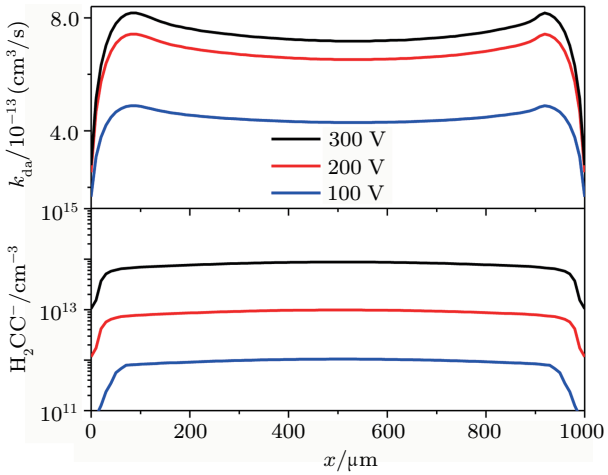


Fig. 7. (color online) The spatial variation profiles of the negative ion (H_2CC^-) and the corresponding attachment coefficient k_{da} at different applied voltage, with $V = 100$, 200, and 300 V.

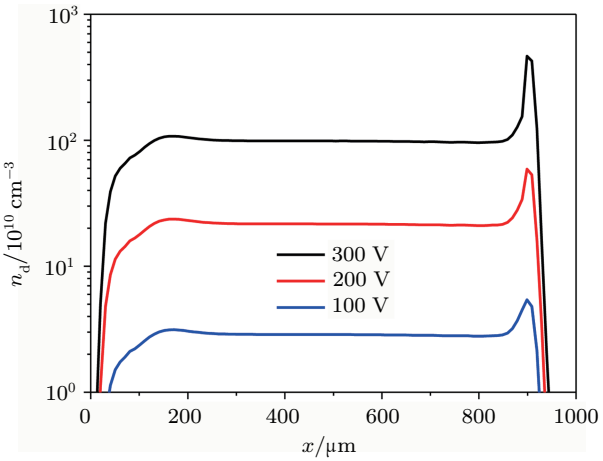


Fig. 8. (color online) The spatial variation profiles of the nanoparticle number density n_d at different applied voltage, with the settings the same as those in Fig. 7.

4. Concluding remarks

The behavior of nanoparticles in atmosphere microdischarges is carefully investigated by using a self-consistent coupling between an aerosol dynamics model and one-dimensional hydrodynamic model. In these MDs, the neutral flow cannot be ignored since the thermophoresis force has a great impact on the distribution of nanoparticle density. Thus, the flow equation and heat transfer equation for neutral gas are carefully investigated. From the standard model, it was found that the secondary electron emissions play a leading role in sustaining discharge.

In this article, the effects of pressure, electrode spacing, and applied voltage on the plasma density and nanoparticle density were studied. We noticed that increasing the electrode spacing, the H_2CC^- density and nanoparticle density decreased instead of increasing, under the influences of secondary electron emissions. However, the pressure has a relatively smaller impact on the nanoparticle density. We have, in particular, discussed the role of applied voltage on the

nanoparticle density, particle size of 10 nm. By varying the applied voltage between 100 V and 300 V, the nanoparticle density increased nearly two orders of magnitude. Hence, the applied voltage can be a very important parameter that can strongly influence the nanoparticle properties, even at moderate voltage differences of 100 V or more.

References

[1] Kogelschatz U 2007 *Contrib. Plasma Phys.* **47** 80
[2] Munoz-Serrano E, Hagelaar G, Callegari Th, Boeuf J and Pitchford L C 2006 *Plasma Phys. Control. Fusion* **48** B391
[3] Kothnur P S, Yuan X H and Raja L L 2003 *Appl. Phys. Lett.* **82** 529
[4] Babayan S E, Jeong J Y, Schutze A, Tu V J, Moravej M, Selwyn G S and Hicks R F 2001 *Plasma Sources Sci. Technol.* **10** 573
[5] Babayan S E, Ding G and Hicks R F 2001 *Plasma Chem. Plasma Process.* **21** 505
[6] Park J, Henins I, Hermann H W, Selwyn G S and Hicks R F 2001 *J. Appl. Phys.* **89** 20
[7] Iza F, Lee J K, and Kong M G 2007 *Phys. Rev. Lett.* **99** 075004
[8] Kwon H, Kim H, Won I, Lee H W, Shin H and Lee J 2013 *Phys. Plasmas* **20** 023506
[9] Radmilovic-Radjenovic M and Radjenovic B 2007 *IEEE Trans. Plasma Sci.* **35** 1223
[10] Belostotskiy S G, Donnelly V M and Economou D J 2008 *Plasma Sources Sci. Technol.* **17** 045018
[11] Kim H C and Lee J K 2004 *Phys. Rev. Lett.* **93** 085003
[12] Kwon H C, Won I H and Lee J K 2001 *Appl. Phys. Lett.* **100** 183702
[13] De Bleecker K, Bogaerts A and Goedheer W 2006 *Phys. Rev. E* **73** 026405
[14] Mao M, Benedikt J, Consoli A and Bogaerts A 2008 *J. Phys. D: Appl. Phys.* **41** 225201
[15] Wetering F, Beckers J and Kroesen G 2012 *J. Phys. D: Appl. Phys.* **45** 485205
[16] Greiner F, Carstensen J, Köler N, Pilch I, Ketelsen H, Knist S and Piel A 2012 *Plasma Sources Sci. Technol.* **21** 065005
[17] Lieberman M A and Lichtenberg A J 2005 *Principles of Plasma Discharges and Materials Processing*, 2nd edn. (New York: Wiley-Interscience)
[18] Liu X M, Li Q N and Xu X 2014 *Chin. Phys. B* **23** 085202
[19] Liu X M, Li Q N and Li R 2015 *Chin. Phys. B* **24** 075204
[20] Moravej M 2006 *Plasma Sourcs Sci. Technol.* **15** 204